

NANO EXPRESS

Open Access



# Heating Efficiency of Triple Vortex State Cylindrical Magnetic Nanoparticles

De Wei Wong<sup>1</sup>, Wei Liang Gan<sup>1</sup>, Yuan Kai Teo<sup>2</sup> and Wen Siang Lew<sup>1\*</sup>

## Abstract

A well-established method for treating cancerous tumors is magnetic hyperthermia, which uses localized heat generated by the relaxation mechanism of magnetic nanoparticles (MNPs) in a high-frequency alternating magnetic field. In this work, we investigate the heating efficiency of cylindrical NiFe MNPs, fabricated by template-assisted pulsed electrodeposition combined with differential chemical etching. The cylindrical geometry of the MNP enables the formation of the triple vortex state, which increases the heat generation efficiency by four times. Using time-dependent calorimetric measurements, the specific absorption rate (SAR) of the MNPs was determined and compared with the numerical calculations from micromagnetic simulations and vibrating sample magnetometer measurements. The magnetization reversal of high aspect ratios MNPs showed higher remanent magnetization and low-field susceptibility leading to higher hysteresis losses, which was reflected in higher experimental and theoretical SAR values. The SAR dependence on magnetic field strength exhibited small SAR values at low magnetic fields and saturates at high magnetic fields, which is correlated to the coercive field of the MNPs and a characteristic feature of ferromagnetic MNPs. The optimization of cylindrical NiFe MNPs will play a pivotal role in producing high heating performance and biocompatible magnetic hyperthermia agents.

**Keywords:** Magnetic nanoparticles, Magnetic hyperthermia, Specific absorption rate, HeLa cells

## Introduction

The applications for magnetic nanoparticles (MNPs) have been extensively researched in biomedical fields, such as magneto-mechanical cell destruction [1–4], magnetic resonance imaging [5–7], drug delivery [8–10], and magnetic hyperthermia [11–14], to compensate for the drawbacks of current diagnosis and therapy methods. The greatest advantage of MNPs is that they can be controlled remotely by an external magnetic field. The resultant magnetic response can be in the form of heat dissipation or magnetic torque, which is dependent on the applied magnetic field configuration and magnetization dynamics of the MNPs [15].

However, different biomedical applications require specific rotation mechanisms in diverse magnetic field configurations. Bio-sensors for cancer bio-markers use magnetic spectroscopy of the MNPs' Brownian motion to measure the bound fraction and relaxation times of

the MNPs within seconds [16]. In magnetic particle imaging for quantifying MNP concentrations, it requires Néel relaxation of the MNPs, while Brownian relaxation, caused by MNPs size distributions, should be minimized [17]. The two mechanisms that exist for the MNPs relaxation processes are Néel and Brownian relaxation, which results in either heat dissipation or spatial rotation of the MNPs. Néel relaxation is correlated to the re-orientation of the MNP magnetic moment to the magnetic field, while Brownian relaxation is correlated to the spatial rotation of the MNP [18–20].

Néel ( $t_N$ ) and Brownian ( $t_B$ ) relaxation time are given by:

$$t_N = t_0 e^{\frac{KV}{k_B T}} \text{ and } t_B = \frac{3\eta V}{k_B T}$$

where  $\eta$  is the viscosity coefficient,  $t_0$  is the inverse attempt frequency,  $K$  is the magnetic anisotropy constant,  $V$  is the volume of MNPs,  $k_B$  is the Boltzmann constant, and  $T$  is the temperature. In principle, the faster mechanism dominates, but both Néel and Brownian

\* Correspondence: [wensiang@ntu.edu.sg](mailto:wensiang@ntu.edu.sg)

<sup>1</sup>School of Physical and Mathematical Sciences, Nanyang Technological University, 21 Nanyang Link, Nanyang 637371, Singapore  
Full list of author information is available at the end of the article

mechanisms can occur concurrently, coupled through heat dissipation and magnetic torque [21]. The effective relaxation time ( $t_{eff}$ ) is given by:

$$\frac{1}{t_{eff}} = \frac{1}{t_B} + \frac{1}{t_N}$$

In smaller MNPs, the dominant mechanism is Néel relaxation, while for larger MNPs it is Brownian relaxation. In Néel relaxation, the MNP magnetization changes direction due to the reconfiguration of its magnetic moment and is dependent on the MNP size and the temperature. While in Brownian relaxation, the MNPs undergo a spatial rotation and are dependent on external conditions, such as viscosity and chemical binding [22–24]. Therefore, it is important to understand the contributions of these magnetic relaxation mechanisms in order to tune and adapt the design of the MNPs to obtain the optimal heat generation for magnetic hyperthermia or magnetic torque for magneto-actuated cell death.

Magnetic hyperthermia is a well-established cancer treatment technique which employs the use of localized heating by MNPs under a high-frequency alternating magnetic field, to induce cancer cell apoptosis and tumor regression [3, 25–27]. In an alternating magnetic field, the heat dissipated by the MNPs in one magnetic field cycle equals to the area of the hysteresis loop  $A$ , given by:

$$A = \int_{-H_{max}}^{+H_{max}} \mu_0 M(H) dH$$

where  $M$  is the magnetization of MNPs, under an alternating magnetic field with frequency  $f$  and amplitude  $\mu_0 H_{max}$  [28–30]. To maintain a low MNPs dose and short treatment duration in magnetic hyperthermia, the MNPs heating efficiency must be maximized. The measurement of MNPs heating performance is referred to as specific absorption rate (SAR), which is given by the heat dissipated per unit of mass of MNPs ( $\text{Wg}^{-1}$ ):

$$\text{SAR} = \frac{Af}{\rho}$$

where  $\rho$  is the density of MNPs.

The efficiency of heat dissipation of MNPs can be experimentally measured in terms of SAR, which is the energy dissipated per unit of mass of MNPs ( $\text{Wg}^{-1}$ ), and is given by:

$$\text{SAR} = C \frac{\Delta T}{\Delta t} \frac{1}{m_{\text{MNP}}}$$

where  $C$  is the specific heat of the medium ( $C_{\text{water}} = 4.18 \text{ Jg}^{-1} \text{ } ^\circ\text{C}^{-1}$ ),  $\Delta T/\Delta t$  is the initial slope of the time against temperature graph, and  $m_{\text{MNP}}$  is the mass of the

MNPs. However, SAR values are not fully representative of the heating efficiency of MNPs as heat dissipation is also influenced by frequency  $f$  and magnetic field strength  $H$ . Hence, effective specific absorption rate or intrinsic loss power (ILP) is used to characterize the MNPs heating efficiency, given by:

$$\text{ILP} = \frac{\text{SAR}}{H^2 f}$$

In cylindrical NiFe MNPs, a triple vortex state is formed, in which clockwise and anti-clockwise vortices are connected at the center of the MNP via a third vortex core, resulting in a three-dimensional magnetization configuration. The theoretical heat dissipation from the MNPs for magnetic hyperthermia applications was calculated from the simulated hysteresis loops and vibrating sample magnetometer measurements. Using time-dependent calorimetric measurements, the specific absorption rate and intrinsic loss power of the MNPs were determined and compared with the numerical calculations.

## Methods

### Fabrication of Magnetic Nanoparticles

Template-assisted pulsed electrodeposition with differential chemical etching is a simple and inexpensive fabrication method to produce MNPs of various compositions, Ni, Fe, or Co. Ni<sub>80</sub>Fe<sub>20</sub>, Permalloy, is a ferromagnetic material that displays exceptional magnetic properties such as high permeability, low coercivity, and near-zero magnetostriction. The fabrication of cylindrical MNPs starts by growing compositionally modulated cylindrical NiFe nanowires using anodic aluminum oxide (AAO) template-assisted pulsed electrodeposition in an electrolyte bath consisting of NiSO<sub>4</sub>, FeSO<sub>4</sub>, and H<sub>3</sub>BO<sub>3</sub> [31–35]. Subsequently, the nanowires were released by dissolving the AAO template in NaOH. Finally, the Fe-rich regions in the nanowires were chemically etched by diluting HNO<sub>3</sub> to form the MNPs. The diameter of the MNPs was determined by the AAO template pore size, while the length was controlled by the high-potential pulse  $V_H$  duration Additional file 1.

### Cell Viability

HeLa cells were seeded into 12-well microtiter plate at  $8 \times 10^4$  cells/well and incubated in Dulbecco's Modified Eagle's medium supplemented with 4.5 g/L glucose, 2 mM L-glutamine, 10% fetal bovine serum, and 1% penicillin/streptomycin in a humidified atmosphere at 37 °C and 5% CO<sub>2</sub>. The cell viability was determined using PrestoBlue, a permeable resazurin-based cell viability reagent, which uses the reducing power of viable cells to quantitatively measure cell proliferation. HeLa cells treated with 0.1 mg/ml of MNPs were incubated with the PrestoBlue reagent at 37 °C and 5% CO<sub>2</sub> for 2 h. The

absorbance values at 570 nm and 600 nm were measured by Tecan Infinite M200 PRO Microplate Reader. The cell viability was expressed as a percentage relative to the cells unexposed to the MNPs. Each experiment was performed in quadruplicate sets of experimental and control assays.

### Statistical Analysis

The results were represented as the mean  $\pm$  standard deviation (SD). Statistical significance was analyzed using one-way analysis of variance (ANOVA) with OriginPro, OriginLab. A  $p$  value of  $< 0.05$  was considered to be statistically significant.

### Micromagnetic Simulations

The magnetization configurations of the MNPs were investigated using a GPU-accelerated micromagnetic simulation program, MuMax3, to solve the Landau–Lifshitz–Gilbert (LLG) equation in three dimensions [36]. These micromagnetic simulations provided insights into the magnetization configurations of the MNP at the microscopic level, which showed the correlation between analytical models and observations from experimental results. The total energy of a system is described by:

$$E_{\text{Total}} = E_{\text{Exchange}} + E_{\text{Anisotropy}} + E_{\text{Zeeman}} + E_{\text{Dipolar}}$$

$$= - \int \mu_0 H_{\text{eff}}(r) \cdot M(r) d^3r$$

where  $H_{\text{eff}} = -\frac{1}{\mu_0} \nabla_M E$ . The Landau–Lifshitz–Gilbert (LLG) equation describes the precession of magnetization  $M$  in an effective magnetic field  $H_{\text{eff}}$  with damping  $\alpha$ .

$$\frac{dM(r)}{dt} = -\gamma M(r) \times H_{\text{eff}}(r) - \frac{\alpha}{M_s} M(r) \times (M(r) \times H_{\text{eff}}(r))$$

where  $\gamma M(r) \times H_{\text{eff}}(r)$  is the precession of  $M(r)$  in a local field  $H_{\text{eff}}(r)$  and  $\frac{\alpha}{M_s} M(r) \times (M(r) \times H_{\text{eff}}(r))$  is the empirical damping term. The material parameters for Permalloy  $\text{Ni}_{80}\text{Fe}_{20}$  were used: saturation magnetization  $M_s$  of  $860 \times 10^3$  A/m, exchange stiffness constant  $A_{\text{ex}}$  of  $1.3 \times 10^{-11}$  J/m, zero magneto-crystalline anisotropy  $k = 0$ , and Gilbert damping constant  $\alpha$  of 0.01. A cell size of  $5 \text{ nm} \times 5 \text{ nm} \times 5 \text{ nm}$  was used for all simulations, which is sufficiently small as compared with the exchange length.

### Experimental Setup for Magnetic Hyperthermia

SAR was experimentally obtained from time-dependent calorimetric measurements by exposing the MNPs to an alternating magnetic field generated by a high-frequency induction heater. MNPs in aqueous suspension with concentrations of 0.05–0.1 mg/ml were poured into a falcon tube, which was insulated by styrofoam and

surrounded by the induction coils. The temperature of the coils was maintained at  $28.0 \pm 0.5$  °C by a water recirculating chiller. The initial temperature of the suspension was maintained at  $28.0 \pm 0.5$  °C for 1 min to eliminate any heat contributions from the induction coils. An alternating magnetic field range of 15.9 to 47.8  $\text{kAm}^{-1}$  and fixed frequency of 360 kHz were applied, within the criterion for clinical magnetic hyperthermia.

## Results and Discussion

### Characterization of Magnetic Nanoparticles

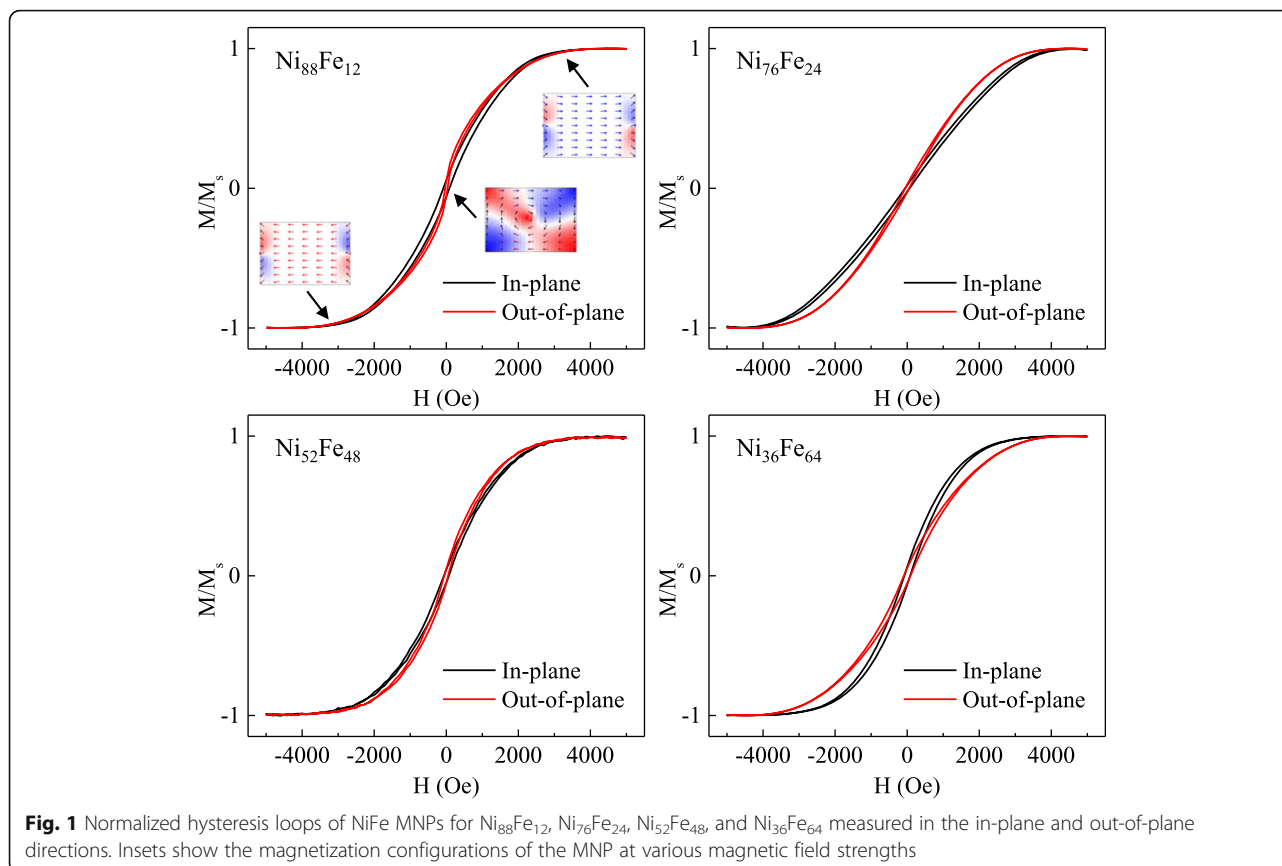
The composition of the fabricated cylindrical NiFe MNPs is determined by  $V_H$  or the electrolyte composition. To show the large degree of control in the MNPs composition, various compositions of MNPs have fabricated ( $\text{Ni}_{88}\text{Fe}_{12}$ ,  $\text{Ni}_{76}\text{Fe}_{24}$ ,  $\text{Ni}_{52}\text{Fe}_{48}$ , and  $\text{Ni}_{36}\text{Fe}_{64}$ ) and verified by energy-dispersive X-ray spectroscopy (EDX). Figure 1 shows the normalized hysteresis loop obtained by vibrating sample magnetometer (VSM) measurements for the NiFe MNPs with various compositions. The magnetic field is increased to a value that is sufficient to overcome the effective magnetic anisotropy such that the magnetization reaches saturation. The squareness ratio SQR is a basic measurement of how square the hysteresis loop is, given by:

$$\text{SQR} = \frac{M_r}{M_s}$$

The values of coercivity  $H_c$  and squareness  $\text{SQR} = M_r/M_s$  for in-plane and out-of-plane applied magnetic fields are tabulated in Table 1. In general, the trend of in-plane  $H_c$  is higher than the out-of-plane  $H_c$  for Ni-rich MNPs ( $\text{Ni}_{88}\text{Fe}_{12}$ ,  $\text{Ni}_{76}\text{Fe}_{24}$ , and  $\text{Ni}_{52}\text{Fe}_{48}$ ), but reversed for Fe-rich MNPs ( $\text{Ni}_{36}\text{Fe}_{64}$ ), which is in agreement with the previous studies on anomalous co-deposition of NiFe nanowires [37].

### Biocompatible Surface Coating

NiFe MNPs tend to aggregate due to the effects of strong dipole interactions between neighboring MNPs. Therefore, the surface modification of the MNPs using biocompatible and biodegradable polymer [38, 39], such as chitosan [40–42], polyvinyl alcohol [43–45], oleic acid [46–48], dextran [49, 50], and most commonly polyethylene glycol (PEG) [51–56], has been proposed. PEG is a hydrophilic polymer that has been widely used for improving blood circulation of liposomes and MNPs [57–60]. To disperse the cylindrical NiFe MNPs into water, a biocompatible  $5000 \text{ g mol}^{-1}$  PEG was used as a stabilizer [61]. The scanning electron microscopy (SEM) image shows the formation of an oxide shell around the MNPs, shown in Fig. 2a. This oxide shell prevents oxidation of the magnetic materials in the MNPs. Previous research works on



FeCo MNPs and Fe MNPs have shown severe oxidation from just exposure to the atmosphere [61, 62].

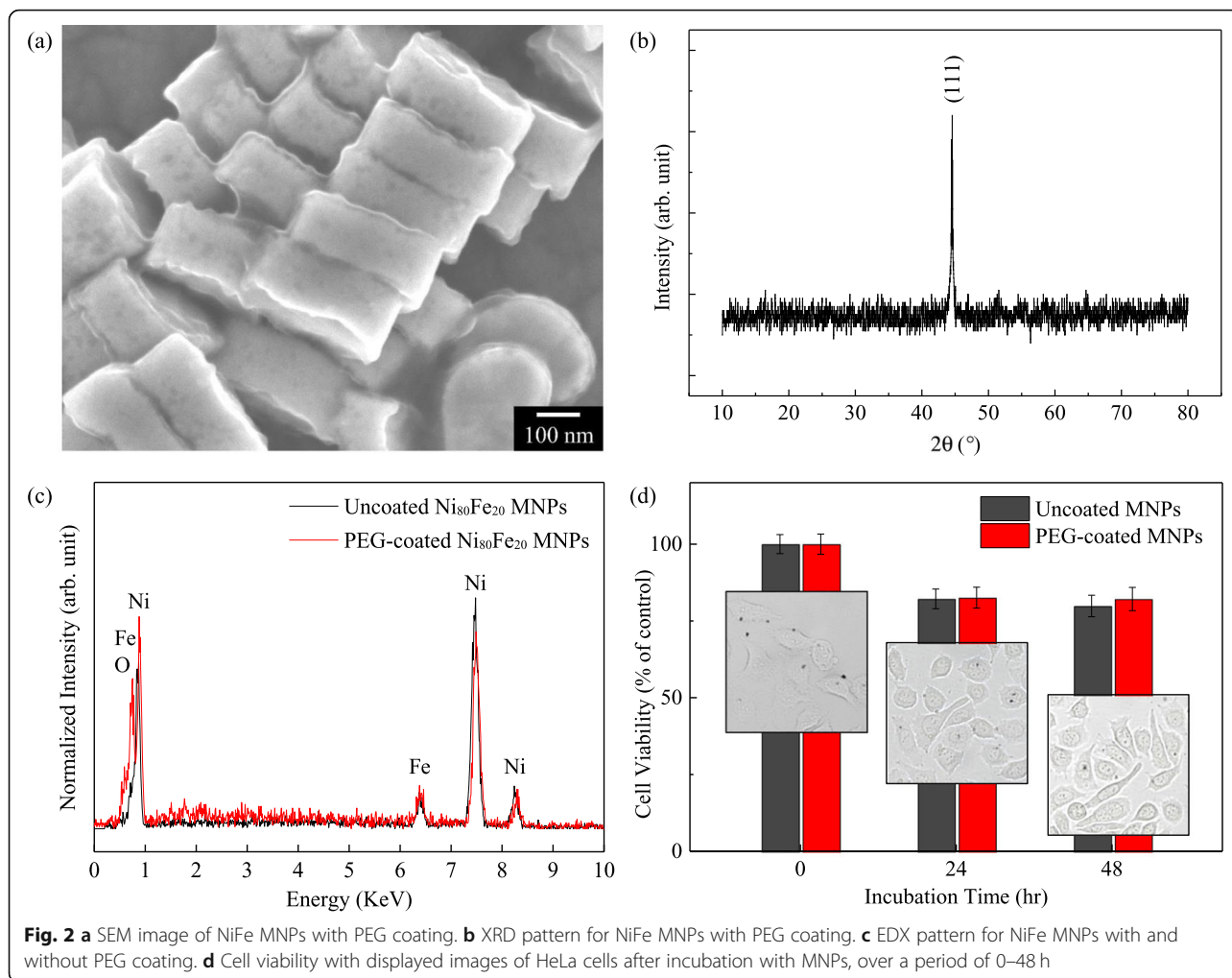
The X-ray diffraction (XRD) pattern peak was mainly indexed at the (111) crystal planes which corresponds to the face-centered cubic (fcc) structure of bulk NiFe, as shown in Fig. 2b. This indicates that the MNPs were electrodeposited with a preferred orientation of (111), which is also evident in NiFe nanowires fabricated by electrodeposition or sputtering [63, 64]. In addition, there was an absence of diffraction peaks corresponding to spinel oxide ( $(\text{NiFe})_3\text{O}_4$ ), which results from the formation of oxide phases due to the high concentration of Fe [65]. The high crystallinity of the NiFe MNPs led to negligible surface spin canting and hence retained the high saturation magnetization and small coercivity of the MNPs. Further

characterizations for the PEG-coated NiFe MNPs were conducted using EDX measurement. As shown in Fig. 2c, mainly of Ni and Fe elements were detected, with the presence of a small percent of O element, an indication of the oxide shell formed around the MNPs.

From Fig. 2d, the cell viability of the HeLa cells exposed to uncoated and PEG-coated NiFe MNPs after 24 h is 82.2% and 82.6%, respectively. After 48 h, the cell viabilities decreased slightly to 79.9% and 82.1%, displaying slightly higher biocompatibility for PEG-coated MNPs. NiFe MNPs without any shells are toxic to mammalian cells and will affect cell viability. The PEG coating was highly biocompatible and can decrease the cytotoxicity and internalization of MNPs into the cells due to endocytosis [66, 67]. The cytotoxicity of the cylindrical NiFe MNPs to HeLa cells is comparable with other commercially available

**Table 1** Coercivity  $H_c$  and squareness  $\text{SQR} = M_r/M_s$  values of NiFe MNPs for  $\text{Ni}_{88}\text{Fe}_{12}$ ,  $\text{Ni}_{76}\text{Fe}_{24}$ ,  $\text{Ni}_{52}\text{Fe}_{48}$ , and  $\text{Ni}_{36}\text{Fe}_{64}$

| Ni:Fe ratio                    | In-plane $H_c$ (Oe) | Out-of-plane $H_c$ (Oe) | In-plane SQR | Out-of-plane SQR |
|--------------------------------|---------------------|-------------------------|--------------|------------------|
| $\text{Ni}_{88}\text{Fe}_{12}$ | 84.5                | 33.8                    | 0.060        | 0.054            |
| $\text{Ni}_{76}\text{Fe}_{24}$ | 62.7                | 54.0                    | 0.023        | 0.027            |
| $\text{Ni}_{52}\text{Fe}_{48}$ | 68.6                | 51.4                    | 0.048        | 0.049            |
| $\text{Ni}_{36}\text{Fe}_{64}$ | 80.7                | 91.1                    | 0.064        | 0.054            |



ferromagnetic NPs used in magnetic hyperthermia research [68].

### Magnetization Dynamics

The composition of the MNPs was kept at Permalloy  $\text{Ni}_{80}\text{Fe}_{20}$ , while the length ( $l$ ) and diameter ( $d$ ) of the MNPs were varied. The exchange energy, demagnetization, or dipolar energy and Zeeman energy contributions to the total energy of the MNP are plotted as a function of applied magnetic field  $H$  along the MNP long axis in Fig. 3a–d, respectively. The MNP was first saturated by a strong magnetic field parallel to its long axis. At large magnetic fields, the Zeeman energy contribution predominates and the spins are mostly aligned in the magnetic field direction. This parallel arrangement of the spins to the field minimizes the exchange energy contribution to the total magnetic energy. As the applied magnetic field is reduced, a clockwise and an anti-clockwise vortex nucleation occur at the ends of the MNP, which progress towards the center of the MNP, leading to a gradual reduction of the parallel magnetization component that causes a drop in the Zeeman contribution,

while other contributions become increasingly significant. The magnetization of the MNP tries to minimize the stray field, and thus reducing its demagnetization energy. At sufficiently low magnetic fields, the triple vortex state is formed, which is a stable magnetization configuration, with total energy kept at a minimum. As the magnetic field reverses, the sharp drop in exchange energy corresponds to the abrupt splitting of the two vortices.

MNPs with different lengths ( $l$ ) were found to have significantly different magnetization configurations. At lengths  $l$  below 100 nm, only a single vortex was nucleated, which is an in-plane and closed flux domain structure, owing to the interaction between the magnetostatic energy and exchange energy. For  $l$  above 100 nm, a pair of anti-clockwise and clockwise vortex cores at the ends of the MNP were nucleated—double vortex state. When the magnetic field decreases, one of the vortex is annihilated, collapsing into the single vortex state. However, at  $l$  above 300 nm, there is no annihilation of vortex at low fields, instead an additional third vortex core was nucleated on the curved surface of the MNP—triple vortex state.

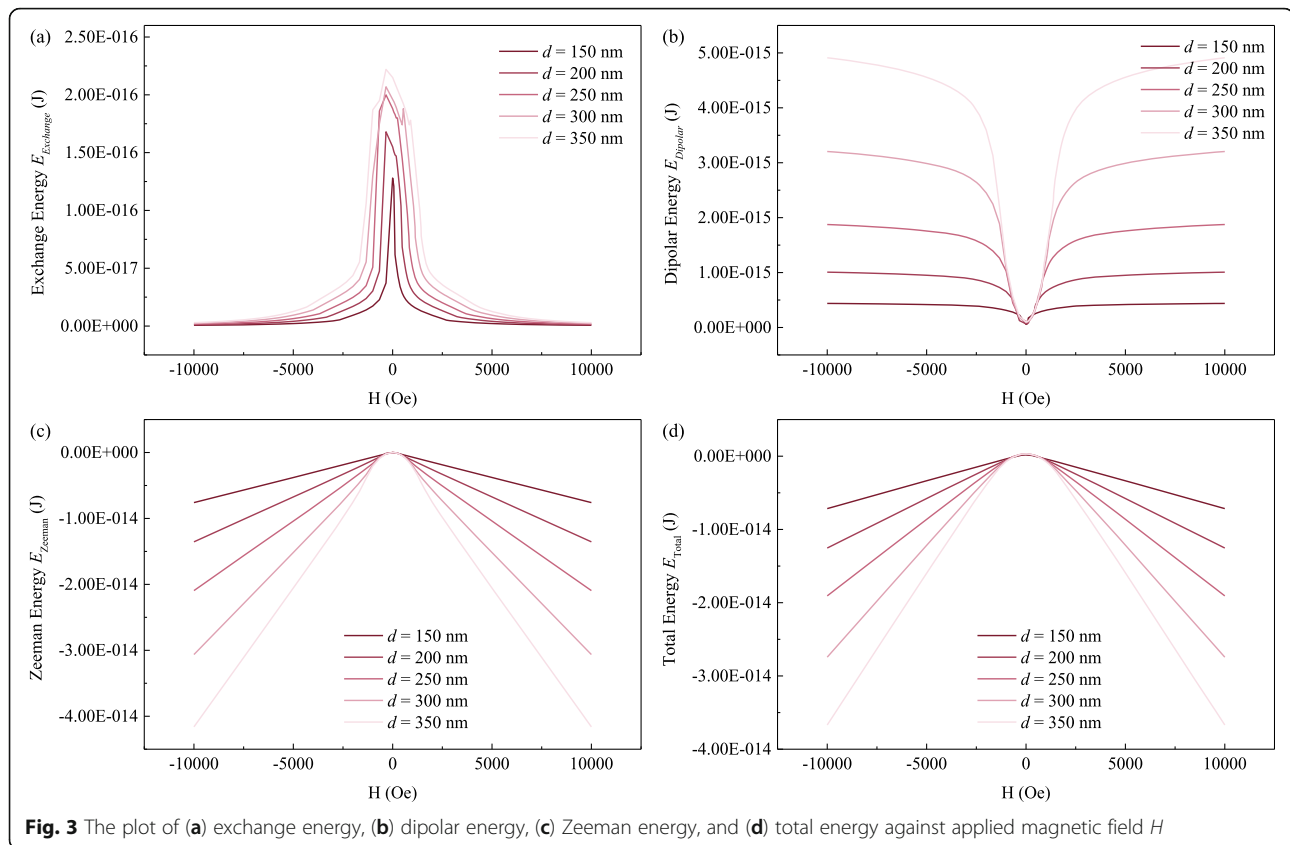


**Fig. 3** The plot of (a) exchange energy, (b) dipolar energy, (c) Zeeman energy, and (d) total energy against applied magnetic field  $H$

### Calorimetric Measurements

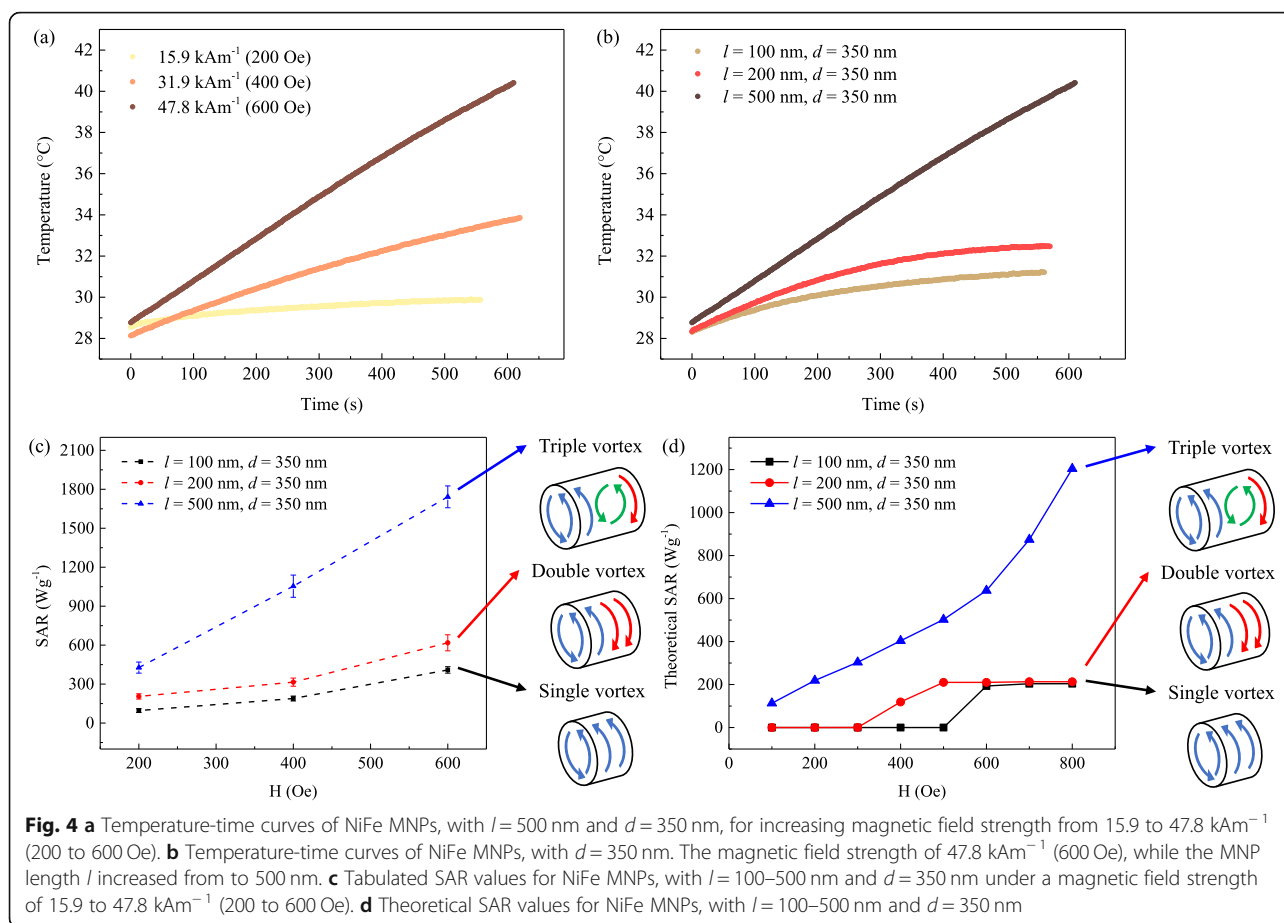
The  $\text{Ni}_{80}\text{Fe}_{20}$  MNPs, with  $l = 500$  nm and  $d = 350$  nm, were exposed to an alternating magnetic field of 15.9 to 47.8  $\text{kAm}^{-1}$  (200 to 600 Oe), and the temperature-time curve is displayed in Fig. 4a. As characterized by the SAR equation, the SAR values were calculated to be 427  $\text{Wg}^{-1}$ , 1054  $\text{Wg}^{-1}$ , and 1742  $\text{Wg}^{-1}$ , for 15.9  $\text{kAm}^{-1}$ , 31.9  $\text{kAm}^{-1}$ , and 47.8  $\text{kAm}^{-1}$ , respectively. As predicted, the larger the magnetic field strength, the greater the SAR value, i.e., the SAR value was proportional to the magnetic field strength. Therefore, ILP was obtained to give a better evaluation of the heating efficiency of the MNPs for magnetic hyperthermia. As characterized by the ILP equation, the ILP values were calculated to be 4.69  $\text{nHm}^2\text{kg}^{-1}$ , 2.88  $\text{nHm}^2\text{kg}^{-1}$ , and 2.12  $\text{nHm}^2\text{kg}^{-1}$ , for 15.9  $\text{kAm}^{-1}$ , 31.9  $\text{kAm}^{-1}$ , and 47.8  $\text{kAm}^{-1}$  at 360 kHz, respectively.

Next, NiFe MNPs, with  $d = 350$  nm and  $l = 100$ –500 nm, were exposed to an alternating magnetic field of 47.8  $\text{kAm}^{-1}$  (600 Oe), and the temperature-time curve is displayed in Fig. 4b. As characterized by the SAR equation, the SAR values were calculated to be 409  $\text{Wg}^{-1}$ , 618  $\text{Wg}^{-1}$ , and 1742  $\text{Wg}^{-1}$ , for  $l = 100$  nm, 200 nm, and 500 nm at 47.8  $\text{kAm}^{-1}$  and 360 kHz, respectively. As characterized by the ILP equation, the ILP values were calculated to be 0.50  $\text{nHm}^2\text{kg}^{-1}$ , 0.75  $\text{nHm}^2\text{kg}^{-1}$ , and

2.12  $\text{nHm}^2\text{kg}^{-1}$  for  $l = 100$  nm, 200 nm, and 500 nm at 47.8  $\text{kAm}^{-1}$  and 360 kHz, respectively.

MNPs with  $l = 500$  nm had far greater heating efficiency than MNPs with  $l = 100$  nm and 200 nm, leading to a more significant temperature rise. The highest SAR value of MNPs with  $l = 500$  nm was 1742  $\text{Wg}^{-1}$  at 47.8  $\text{kAm}^{-1}$  and 360 kHz. For comparison, the SAR values for magnetic field of 15.9 to 31.9  $\text{kAm}^{-1}$  (200 to 400 Oe) and MNPs with  $d = 350$  nm and  $l = 100$ –500 nm were tabulated in Fig. 4c. Under the same conditions, the SAR and ILP values of MNPs with  $l = 500$  nm were four times higher than those with MNPs of smaller  $l$ . From micromagnetic simulations, it was observed that as  $l$  increases to  $> 300$  nm, the magnetization reversal process of the MNP changed from a double vortex state to triple vortex state. At  $l < 300$  nm, only a single vortex state or double vortex state was observed. The remanent magnetization  $M_r$  of the MNP was significantly higher for the triple vortex state as compared with the single or double vortex state.

For single domain MNPs, the theoretical model to calculate the dynamic hysteresis loop has been proposed by Carrey et al. [69] For multi-domains MNPs, the use of micromagnetic simulations to obtain static hysteresis loop for calculation was reasonable for MNPs with large sizes, above the critical size for superparamagnetism, as



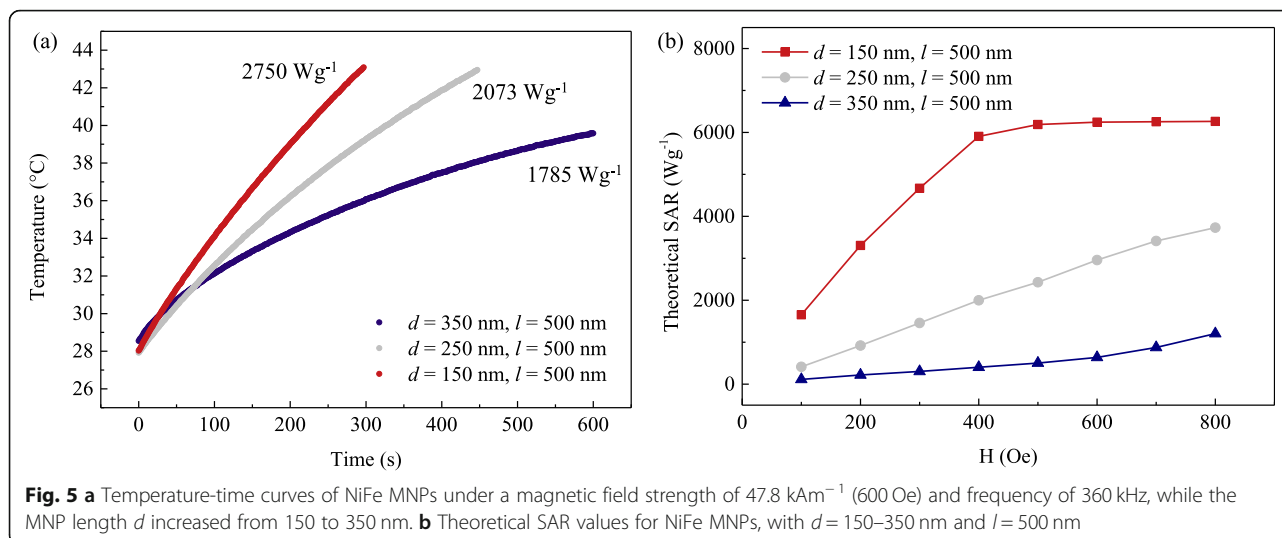
the switching time of the magnetization is in the order of  $10^{-9}$  s. Since the switching time of magnetic hyperthermia is in the order  $\sim 10^{-6}$  s, the large MNPs are able to keep up with the alternating magnetic field. The area of hysteresis loops obtained from micromagnetic simulations of cylindrical NiFe MNPs and VSM measurements was used to theoretically calculate the SAR values and tabulated in Fig. 4d.

The SAR values of MNPs with  $l = 100$  nm and 200 nm displayed a small SAR value at low magnetic fields below  $H_c$  and sharply increased until it reaches a saturation at high magnetic fields, which is a characteristic of the ferromagnetic regime. In contrast, the magnetic field dependence of the SAR value of  $l = 500$  nm MNPs, with the triple vortex state, followed a non-linear relationship with SAR values that were  $\sim 6$  times greater. The high remanent magnetization  $M_r$  of the triple vortex state in the  $l = 500$  nm MNPs was evident in the non-zero SAR values at low magnetic fields. The comparison between calorimetric measurements (Fig. 4c) and numerical calculations (Fig. 4d) indicates a qualitative and quantitative agreement on the features of MNPs in the ferromagnetic regime, displaying small SAR values at low magnetic

fields and saturation at high magnetic fields which was correlated to the  $H_c$  of the MNPs.

The heat dissipation of NiFe MNPs with triple vortex states was compared for  $d = 150$ –350 nm, under an alternating magnetic field of 47.8  $\text{kAm}^{-1}$  (600 Oe), and the temperature-time curve is displayed in Fig. 5a. The SAR and ILP values were calculated to be 1785  $\text{Wg}^{-1}$ , 2073  $\text{Wg}^{-1}$ , and 2750  $\text{Wg}^{-1}$  and 2.17  $\text{nHm}^2\text{kg}^{-1}$ , 2.52  $\text{nHm}^2\text{kg}^{-1}$ , and 3.34  $\text{nHm}^2\text{kg}^{-1}$ , for  $d = 350$  nm, 250 nm, and 150 nm, respectively. The MNPs with  $d = 150$  nm and 250 nm were able to reach the optimal therapeutic temperature of 43  $^{\circ}\text{C}$  in 4.92 min and 7.45 min at concentration of 0.1 mg/ml. Comparing MNPs with different aspect ratios, it was observed that the heating efficiency of  $d = 150$  nm MNPs was 1.54 times greater than  $d = 350$  nm MNPs. This was because MNPs with  $d = 150$  nm possessed the highest low-field susceptibility and  $M_r$ . Therefore, the SAR value was closely correlated to the magnetization reversal process of the MNPs with both variations in  $l$  and  $d$ .

From micromagnetic simulations, it can be observed that the area of hysteresis  $A$  evolves significantly with the diameter ( $d$ ) of the MNP. Therefore, the SAR value



of the  $d = 150$  nm MNPs increases so rapidly and saturates at a maximum SAR value of  $6263 \text{ Wg}^{-1}$ . The numerical calculations showed that the MNPs with higher aspect ratios have higher hysteresis losses, resulting in higher theoretical SAR values, as shown in Fig. 5b. The comparison between calorimetric measurements (Fig. 5a) and numerical calculations (Fig. 5b) was in good qualitative agreement, but there were quantitative disagreements in the values of hysteresis losses. The mismatch between the experimental and theoretical values arose from the NiFe MNPs being non-superparamagnetic and possessed non-negligible remanent magnetization, leading to unwanted agglomeration due to strong magnetic dipole interactions between neighboring MNPs [70, 71]. Since hydrodynamic volume of MNPs is a component governing the Brownian motion, the extent of aggregation of the MNPs will determine the dominating relaxation mechanism, i.e., Néel or Brownian relaxation. Hence, an aggregated group of MNPs versus a single free MNP will greatly differ in SAR values. Furthermore, an alternating magnetic field can induce nano-columns or nano-chains formation which exhibit dissimilar Brownian relaxation mechanism and hence accounted for the discrepancy between the experimental and theoretical values [72–74].

## Conclusions

The high SAR values displayed by the cylindrical NiFe MNPs, comparable with iron oxide MNPs (IOMNPs) and superparamagnetic iron oxide nanoparticles (SPIONs) [28, 75], demonstrate the capability of these MNPs in heat dissipation under an alternating magnetic field. MNPs with the triple vortex state had far greater heating efficiency than MNPs with double or single vortex state, which have a SAR value of four times greater, attributed to the high  $M_r$  of the MNPs in the triple vortex state. Comparing MNPs with different aspect ratios, it was observed that the heating

efficiency of  $d = 150$  nm MNPs was 1.54 times greater than  $d = 350$  nm MNPs due to a larger  $M_r$  and low-field susceptibility. Both calorimetric measurements and micromagnetic simulations showed the correlation between the magnetization reversal process and the higher hysteresis losses from  $d = 150$  nm MNPs, resulting in higher experimental and theoretical SAR values. The easy control of the sizes of the MNPs and their magnetic properties indicate great potential for in vivo magnetic hyperthermia cancer therapy trials.

## Supplementary information

Supplementary information accompanies this paper at <https://doi.org/10.1186/s11671-019-3169-6>.

**Additional file 1.** Supplementary Material.

## Abbreviations

$d$ : Diameter of magnetic nanoparticles; EDX: Energy-dispersive X-ray spectroscopy;  $H_c$ : Coercivity; ILP: Intrinsic loss power;  $l$ : Length of magnetic nanoparticles; MNPs: Magnetic nanoparticles;  $M_r$ : Remanent magnetization; PEG: Polyethylene glycol; SAR: Specific absorption rate; SEM: Scanning electron microscopy; SQR: Squareness ratio;  $V_H$ : High-potential electrodeposition pulse; VSM: Vibrating sample magnetometer; XRD: X-ray diffraction spectroscopy

## Acknowledgements

The work was supported by the Singapore National Research Foundation, Prime Minister's Office under an Industry-IHL Partnership Program (NRF2015-IIP001-001). WSL is also a member of the Singapore Spintronics Consortium (SG-SPIN).

## Authors' Contributions

D.W.W. and W.L.G. performed the micromagnetic simulations and calorimetric measurements. D.W.W. and Y.K.T. performed the in vitro cell experiments. The project was supervised by W.S.L. All authors discussed the results and contributed to the manuscript. All authors read and approved the final manuscript.

## Availability of Data and Materials

The datasets generated during and/or analyzed during the current study are available from the corresponding author on reasonable request.

**Competing Interests**

The authors declare that they have no competing interests.

**Author details**

<sup>1</sup>School of Physical and Mathematical Sciences, Nanyang Technological University, 21 Nanyang Link, Nanyang 637371, Singapore. <sup>2</sup>School of Biological Sciences, Nanyang Technological University, 60 Nanyang Drive, Nanyang 637551, Singapore.

Received: 18 January 2019 Accepted: 1 October 2019

Published online: 16 December 2019

**References**

- Kim D-H, Rozhkova EA, Ulasov IV, Bader SD, Rajh T, Lesniak MS et al (2010) Biofunctionalized magnetic-vortex microdiscs for targeted cancer-cell destruction. *Nat Mater* 9(2):165–171
- Chiriac H, Radu E, Tibu M, Stoian G, Ababei G, Lăbușcă L et al (2018) Fe-Cr-Nb-B ferromagnetic particles with shape anisotropy for cancer cell destruction by magneto-mechanical actuation. *Sci Rep* 8(1):11538
- Golovin YI, Gribanovsky SL, Golovin DY, Klyachko NL, Majouga AG, Master AM et al (2015) Towards nanomedicines of the future: remote magneto-mechanical actuation of nanomedicines by alternating magnetic fields. *J Control Release* 219:43–60
- Martínez-Banderas AI, Aires A, Teran FJ, Perez JE, Cadenas JF, Alsharif N et al (2016) Functionalized magnetic nanowires for chemical and magneto-mechanical induction of cancer cell death. *Sci Rep* 6:35786
- Lévy M, Lagarde F, Maralioi V-A, Blanchin M-G, Gendron F, Wilhelm C et al (2010) Degradability of superparamagnetic nanoparticles in a model of intracellular environment: follow-up of magnetic, structural and chemical properties. *Nanotechnology* 21(39):395103
- Elias A, Tsourkas A (2009) Imaging circulating cells and lymphoid tissues with iron oxide nanoparticles. *ASH Education Program Book* 2009(1):720–726
- Vitaliano G, Kim J, Mintzopoulos D, Adam C, Vitaliano F, Lukas S et al (2018) Novel targeted clathrin-based superparamagnetic iron oxide nanoparticles for CNS magnetic resonance imaging of dopamine transporters. *Biol Psychiatry* 83(9):S450
- Tietze R, Zaloga J, Unterweger H, Lyer S, Friedrich RP, Janko C et al (2015) Magnetic nanoparticle-based drug delivery for cancer therapy. *Biochem Biophys Res Commun* 468(3):463–470
- Chertok B, Moffat BA, David AE, Yu F, Bergemann C, Ross BD et al (2008) Iron oxide nanoparticles as a drug delivery vehicle for MRI monitored magnetic targeting of brain tumors. *Biomaterials* 29(4):487–496
- Inozemtseva OA, German SV, Navolokin NA, Bucharskaya AB, Maslyakova GN, Gorin DA (2018) Chapter 6 - encapsulated magnetite nanoparticles: preparation and application as multifunctional tool for drug delivery systems. In: Nikolelis DP (ed) Nikoleli G-P, editors. Elsevier, Nanotechnology and Biosensors, pp 175–192
- Yang Y, Liu X, Lv Y, Herng TS, Xu X, Xia W et al (2015) Orientation mediated enhancement on magnetic hyperthermia of Fe<sub>3</sub>O<sub>4</sub> Nanodisc. *Adv Funct Mater* 25(5):812–820
- Yang Y, Liu X, Yang Y, Xiao W, Li Z, Xue D et al (2013) Synthesis of nonstoichiometric zinc ferrite nanoparticles with extraordinary room temperature magnetism and their diverse applications. *J Mater Chem C* 1(16):2875
- Bellizzi G, Bucci OM (2018) Magnetic nanoparticle hyperthermia. In: Crocco L, Karanasiou I, James ML, Conceição RC (eds) Emerging electromagnetic technologies for brain diseases diagnostics, monitoring and therapy. Springer International Publishing, Cham, pp 129–191
- Thiesen B, Jordan A (2008) Clinical applications of magnetic nanoparticles for hyperthermia. *Int J Hyperth* 24(6):467–474
- Maier-Hauff K, Ulrich F, Nestler D, Niehoff H, Wust P, Thiesen B et al (2011) Efficacy and safety of intratumoral radiotherapy using magnetic iron-oxide nanoparticles combined with external beam radiotherapy on patients with recurrent glioblastoma multiforme. *J Neuro-Oncol* 103(2):317–324
- Zhang X, Reeves DB, Perreard IM, Kett WC, Griswold KE, Gimi B et al (2013) Molecular sensing with magnetic nanoparticles using magnetic spectroscopy of nanoparticle Brownian motion. *Biosens Bioelectron* 50:441–446
- Reeves DB, Weaver JB (2015) Combined Néel and Brown rotational Langevin dynamics in magnetic particle imaging, sensing, and therapy. *Appl Phys Lett* 107(22):223106
- Dieckhoff J, Eberbeck D, Schilling M, Ludwig F (2016) Magnetic-field dependence of Brownian and Néel relaxation times. *J Appl Phys* 119(4):043903
- Reeves DB, Weaver JB (2015) Combined Néel and Brown rotational Langevin dynamics in magnetic particle imaging, sensing, and therapy. *Appl Phys Lett* 107(22):223106
- Weaver JB, Zhang X, Kuehlert E, Toraya-Brown S, Reeves DB, Perreard IM et al (2013) Quantification of magnetic nanoparticles with low frequency magnetic fields: compensating for relaxation effects. *Nanotechnology* 24(32):325502
- Mamiya H, Jeyadevan B (2011) Hyperthermic effects of dissipative structures of magnetic nanoparticles in large alternating magnetic fields. *Sci Rep* 1:157
- Adam MR, Eric WH, John BW (2009) Nanoparticle temperature estimation in combined ac and dc magnetic fields. *Phys Med Biol* 54(19):L51
- Rauwerdink AM, Weaver JB (2010) Viscous effects on nanoparticle magnetization harmonics. *J Magn Magn Mater* 322(6):609–613
- Rauwerdink AM, Weaver JB (2010) Measurement of molecular binding using the Brownian motion of magnetic nanoparticle probes. *Appl Phys Lett* 96(3):033702
- Ling Y, Tang X, Wang F, Zhou X, Wang R, Deng L et al (2017) Highly efficient magnetic hyperthermia ablation of tumors using injectable polymethylmethacrylate-Fe<sub>3</sub>O<sub>4</sub>. *RSC Adv* 7(5):2913–2918
- Zhang W, Zuo X, Niu Y, Wu C, Wang S, Guan S et al (2017) Novel nanoparticles with Cr<sup>3+</sup> substituted ferrite for self-regulating temperature hyperthermia. *Nanoscale* 9(37):13929–13937
- Cabrera D, Lak A, Yoshida T, Matera ME, Ortega D, Ludwig F et al (2017) Unraveling viscosity effects on the hysteresis losses of magnetic nanocubes. *Nanoscale* 9(16):5094–5101
- Hervault A, Thanh NTK (2014) Magnetic nanoparticle-based therapeutic agents for thermo-chemotherapy treatment of cancer. *Nanoscale* 6(20):11553–11573
- Shaterabadi Z, Nabiyouni G, Soleymani M (2017) Physics responsible for heating efficiency and self-controlled temperature rise of magnetic nanoparticles in magnetic hyperthermia therapy. *Prog Biophys Mol Biol* 133:9–19. <https://doi.org/10.1016/j.pbiomolbio.2017.10.001>
- Delavari H, Hosseini HRM, Wolff M (2013) Modeling of self-controlling hyperthermia based on nickel alloy ferrofluids: proposition of new nanoparticles. *J Magn Magn Mater* 335:59–63
- Gan WL, Chandra Sekhar M, Wong DW, Purnama I, Chiam SY, Wong LM et al (2014) Multi-vortex states in magnetic nanoparticles. *Appl Phys Lett* 105(15):152405
- Wong DW, Chandra Sekhar M, Gan WL, Purnama I, Lew WS (2015) Dynamics of three-dimensional helical domain wall in cylindrical NiFe nanowires. *J Appl Phys* 117(17):17A747
- Wong D, Purnama I, Lim G, Gan W, Murapaka C, Lew W (2016) Current-induced three-dimensional domain wall propagation in cylindrical NiFe nanowires. *J Appl Phys* 119(15):153902
- Wong DW, Gan WL, Liu N, Lew WS (2017) Magneto-actuated cell apoptosis by biaxial pulsed magnetic field. *Sci Rep* 7(1):10919
- Wong DW, Gan WL, Teo YK, Lew WS (2018) Interplay of cell death signaling pathways mediated by alternating magnetic field gradient. *Cell Death Dis* 4(1):49
- Vansteenkiste A, Leliaert J, Dvornik M, Helsen M, Garcia-Sanchez F, Van Waeyenberge B (2014) The design and verification of MuMax3. *AIP Adv* 4(10):107133
- Dragos O, Chiriac H, Lupu N, Grigoras M, Tabakovic I (2016) Anomalous codeposition of fcc NiFe nanowires with 5–55% Fe and their morphology, crystal structure and magnetic properties. *J Electrochem Soc* 163(3):D83–D94
- Rai PK, Lee J, Kailasa SK, Kwon EE, Tsang YF, Ok YS et al (2018) A critical review of ferrate (VI)-based remediation of soil and groundwater. *Environ Res* 160:420–448
- Azzouz A, Kailasa SK, Lee SS, Rascón AJ, Ballesteros E, Zhang M et al (2018) Review of nanomaterials as sorbents in solid-phase extraction for environmental samples. *TrAC Trends Anal Chem* 108:347–369. <https://doi.org/10.1016/j.trac.2018.08.009>
- Luo L, Zhu L, Xu Y, Shen L, Wang X, Ding Y et al (2011) Hydrogen peroxide biosensor based on horseradish peroxidase immobilized on chitosan-wrapped NiFe<sub>2</sub>O<sub>4</sub> nanoparticles. *Microchim Acta* 174(1–2):55–61
- Luo L, Li Q, Xu Y, Ding Y, Wang X, Deng D et al (2010) Amperometric glucose biosensor based on NiFe<sub>2</sub>O<sub>4</sub> nanoparticles and chitosan. *Sensors Actuators B Chem* 145(1):293–298

42. Zhou S, Li Y, Cui F, Jia M, Yang X, Wang Y et al (2014) Development of multifunctional folate-poly (ethylene glycol)-chitosan-coated  $\text{Fe}_3\text{O}_4$  nanoparticles for biomedical applications. *Macromol Res* 22(1):58–66
43. Rana S, Gallo A, Srivastava R, Misra R (2007) On the suitability of nanocrystalline ferrites as a magnetic carrier for drug delivery: functionalization, conjugation and drug release kinetics. *Acta Biomater* 3(2):233–242
44. Sivakumar P, Ramesh R, Ramanand A, Ponnusamy S, Muthamizhchelvan C (2011) Synthesis and characterization of nickel ferrite magnetic nanoparticles. *Mater Res Bull* 46(12):2208–2211
45. Sivakumar P, Ramesh R, Ramanand A, Ponnusamy S, Muthamizhchelvan C (2011) Preparation of sheet like polycrystalline  $\text{NiFe}_2\text{O}_4$  nanostructure with PVA matrices and their properties. *Mater Lett* 65(9):1438–1440
46. Tomitaka A, Koshi T, Hatsugai S, Yamada T, Takemura Y (2011) Magnetic characterization of surface-coated magnetic nanoparticles for biomedical application. *J Magn Magn Mater* 323(10):1398–1403
47. Kodama RH, Berkowitz AE, McNiff E Jr, Foner S (1996) Surface spin disorder in  $\text{NiFe}_2\text{O}_4$  nanoparticles. *Phys Rev Lett* 77(2):394
48. Maaz K, Karim S, Mumtaz A, Hasanain S, Liu J, Duan J (2009) Synthesis and magnetic characterization of nickel ferrite nanoparticles prepared by co-precipitation route. *J Magn Magn Mater* 321(12):1838–1842
49. Ayala V, Herrera AP, Latorre-Estevés M, Torres-Lugo M, Rinaldi C (2013) Effect of surface charge on the colloidal stability and in vitro uptake of carboxymethyl dextran-coated iron oxide nanoparticles. *J Nanopart Res* 15(8):1874
50. Khot V, Salunkhe A, Thorat N, Ningthoujam R, Pawar S (2013) Induction heating studies of dextran coated  $\text{MgFe}_2\text{O}_4$  nanoparticles for magnetic hyperthermia. *Dalton Trans* 42(4):1249–1258
51. Phadatare M, Khot V, Salunkhe A, Thorat N, Pawar S (2012) Studies on polyethylene glycol coating on  $\text{NiFe}_2\text{O}_4$  nanoparticles for biomedical applications. *J Magn Magn Mater* 324(5):770–772
52. Islam MN, Abbas M, Kim C (2013) Synthesis of monodisperse and high moment nickel-iron (NiFe) nanoparticles using modified polyol process. *Curr Appl Phys* 13(9):2010–2013
53. Sertkol M, Köseoğlu Y, Baykal A, Kavas H, Başaran A (2009) Synthesis and magnetic characterization of  $\text{Zn}_0.6\text{Ni}_0.4\text{Fe}_2\text{O}_4$  nanoparticles via a polyethylene glycol-assisted hydrothermal route. *J Magn Magn Mater* 321(3):157–162
54. Liu XL, Fan HM, Yi JB, Yang Y, Choo ESG, Xue JM et al (2012) Optimization of surface coating on  $\text{Fe}_3\text{O}_4$  nanoparticles for high performance magnetic hyperthermia agents. *J Mater Chem* 22(17):8235–8244
55. Lee DH, Kang M, Lee HJ, Kim JA, Choi Y-K, Cho H et al (2015) Enhanced cellular uptake of silica-coated magnetite nanoparticles compared with peg-coated ones in stem cells. *J Nanosci Nanotechnol* 15(8):5512–5519
56. Jang D-H, Lee Y-I, Kim K-S, Park E-S, Kang S-C, Yoon T-J et al (2013) Induced heat property of polyethyleneglycol-coated iron oxide nanoparticles with dispersion stability for hyperthermia. *J Nanosci Nanotechnol* 13(9):6098–6102
57. Yu WW, Chang E, Falkner JC, Zhang J, Al-Somali AM, Sayes CM et al (2007) Forming biocompatible and nonaggregated nanocrystals in water using amphiphilic polymers. *J Am Chem Soc* 129(10):2871–2879
58. Sperling RA, Pellegrino T, Li JK, Chang WH, Parak WJ (2006) Electrophoretic separation of nanoparticles with a discrete number of functional groups. *Adv Funct Mater* 16(7):943–948
59. Torchilin VP (2005) Recent advances with liposomes as pharmaceutical carriers. *Nat Rev Drug Discov* 4(2):145
60. Dubertret B, Skourides P, Norris DJ, Noireaux V, Brivanlou AH, Libchaber A (2002) In vivo imaging of quantum dots encapsulated in phospholipid micelles. *Science*. 298(5599):1759–1762
61. Abbas M, Islam MN, Rao BP, Ogawa T, Takahashi M, Kim C (2013) One-pot synthesis of high magnetization air-stable FeCo nanoparticles by modified polyol method. *Mater Lett* 91:326–329
62. Kura H, Takahashi M, Ogawa T (2010) Synthesis of monodisperse iron nanoparticles with a high saturation magnetization using an Fe (CO) x–Oleylamine reacted precursor. *J Phys Chem C* 114(13):5835–5838
63. Salem MS, Sergelius P, Zierold R, Moreno JMM, Görlitz D, Nielsch K (2012) Magnetic characterization of nickel-rich NiFe nanowires grown by pulsed electrodeposition. *J Mater Chem* 22(17):8549–8557
64. Nahrwold G, Scholtyssek JM, Motl-Ziegler S, Albrecht O, Merkt U, Meier G (2010) Structural, magnetic, and transport properties of Permalloy for spintronic experiments. *J Appl Phys* 108(1):013907
65. Chen Y, Luo X, Yue G-H, Luo X, Peng D-L (2009) Synthesis of iron–nickel nanoparticles via a nonaqueous organometallic route. *Mater Chem Phys* 113(1):412–416
66. Gupta AK, Gupta M (2005) Cytotoxicity suppression and cellular uptake enhancement of surface modified magnetic nanoparticles. *Biomaterials*. 26(13):1565–1573
67. Gupta AK, Curtis AS (2004) Lactoferrin and ceruloplasmin derivatized superparamagnetic iron oxide nanoparticles for targeting cell surface receptors. *Biomaterials*. 25(15):3029–3040
68. Tomitaka A, Hirukawa A, Yamada T, Morishita S, Takemura Y (2009) Biocompatibility of various ferrite nanoparticles evaluated by in vitro cytotoxicity assays using HeLa cells. *J Magn Magn Mater* 321(10):1482–1484
69. Carrey J, Mehdaoui B, Respaud M (2011) Simple models for dynamic hysteresis loop calculations of magnetic single-domain nanoparticles: application to magnetic hyperthermia optimization. *J Appl Phys* 109(8):083921
70. Mehdaoui B, Meffre A, Carrey J, Lachaize S, Lacroix LM, Gougeon M et al (2011) Optimal size of nanoparticles for magnetic hyperthermia: a combined theoretical and experimental study. *Adv Funct Mater* 21(23):4573–4581
71. Serantes D, Baldomir D, Martinez-Boubeta C, Simeonidis K, Angelakeris M, Natividad E et al (2010) Influence of dipolar interactions on hyperthermia properties of ferromagnetic particles. *J Appl Phys* 108(7):073918
72. Klokkenburg M, Erné BH, Meeldijk JD, Wiedenmann A, Petukhov AV, Dullens RP et al (2006) In situ imaging of field-induced hexagonal columns in magnetite ferrofluids. *Phys Rev Lett* 97(18):185702
73. Liu C-M, Guo L, Wang R-M, Deng Y, Xu H-B, Yang S (2004) Magnetic nanochains of metal formed by assembly of small nanoparticles. *Chem Commun* 23:2726–2727
74. Mehdaoui B, Meffre A, Lacroix LM, Carrey J, Lachaize S, Gougeon M et al (2010) Large specific absorption rates in the magnetic hyperthermia properties of metallic iron nanocubes. *J Magn Magn Mater* 322(19):L49–L52
75. Iacovita C, Stiufluic R, Radu T, Florea A, Stiufluic G, Dutu A et al (2015) Polyethylene glycol-mediated synthesis of cubic iron oxide nanoparticles with high heating power. *Nanoscale Res Lett* 10(1):391

## Publisher's Note

Springer Nature remains neutral with regard to jurisdictional claims in published maps and institutional affiliations.

**Submit your manuscript to a SpringerOpen<sup>®</sup> journal and benefit from:**

- Convenient online submission
- Rigorous peer review
- Open access: articles freely available online
- High visibility within the field
- Retaining the copyright to your article

Submit your next manuscript at ► [springeropen.com](https://www.springeropen.com)